Journal of Materials Science and Chemical Engineering, 2026, 14(4), 1-19
https://www.scirp.org/journal/msce
ISSN Online: 2327-6053
ISSN Print: 2327-6045

Donor-Doping Optimization of In_2S_3 Buffer Layers in CIGS Solar Cells: A TCAD Diagnostic of Transport-Recombination-Leakage Competition via R_S and R_{sh}

Youssou Gning, Marcel Biagui, Moussa Toure, Aly Toure, Mamadou Lamine Samb*

Department of Physics and Chemistry, University Iba Der Thiam of Thies, Thies, Senegal
Email: *mlsamb@univ-thies.sn

How to cite this paper: Gning, Y., Biagui, M., Toure, M., Toure, A. and Samb, M.L. (2026) Donor-Doping Optimization of In_2S_3 Buffer Layers in CIGS Solar Cells: A TCAD Diagnostic of Transport-Recombination-Leakage Competition via R_s and R_{sh}. *Journal of Materials Science and Chemical Engineering*, **14**, 1-19.
https://doi.org/10.4236/msce.2026.144001

Received: March 2, 2026
Accepted: March 30, 2026
Published: April 2, 2026

Abstract

This work presents a comprehensive numerical study aimed at optimizing the performance of CIGS ($Cu(In, Ga)Se_2$) solar cells incorporating indium sulfide (In_2S_3) as a non-toxic buffer layer alternative to conventional CdS. Two-dimensional simulations were performed using the SILVACO ATLAS device simulator, based on the self-consistent solution of Poisson's equation and carrier continuity equations within the drift-diffusion framework under standard AM1.5G illumination (100 mW·cm^{-2}) at 300 K. The study focuses on the impact of the donor concentration N_D in the In_2S_3 buffer layer, varied from 10^{16} to 7×10^{18} cm^{-3}. Its influence was evaluated through the main photovoltaic parameters: short-circuit current density (J_{SC}), open-circuit voltage (V_{OC}), fill factor (FF), and power conversion efficiency (η), as well as the parasitic resistances (R_s and R_{sh}). The results reveal a non-monotonic dependence of device performance on N_D, highlighting the existence of an optimal trade-off between transport improvement and recombination enhancement. A maximum efficiency of 19.3% is obtained at $N_D = 6 \times 10^{16}$ cm^{-3}. In the low-doping regime (~10^{16} cm^{-3}), the efficiency remains limited (16.6%) mainly due to insufficient buffer-layer conductivity and relatively high series resistance, which constrain carrier extraction and reduce the fill factor. As N_D increases toward the intermediate range (10^{16} to 7×10^{16} cm^{-3}), enhanced conductivity improves electron transport, reduces R_s, and promotes better current collection, leading to simultaneous gains in J_{SC} and FF. Beyond the optimum, however, performance degradation becomes dominant. At higher donor concentrations ($\gtrsim 5 \times 10^{17}$ cm^{-3}), η decreases and stabilizes around 14.0%, corresponding to an overall loss of approximately 27% compared with the optimum. This drop is primarily governed by the strong reduction of V_{OC}, indicating that recombination mech-

anisms increasingly dominate over resistive improvements. Although FF may remain high at large N_D due to reduced R_s and increased R_{sh}, these resistive benefits cannot compensate for the voltage loss. Overall, the analysis confirms that buffer-layer doping must be carefully optimized: moderate doping improves transport, whereas excessive doping irreversibly limits device efficiency by enhancing recombination and reducing V_{OC}.

Keywords

CIGS Solar Cells, In_2S_3 Buffer Layer, Donor Concentration, TCAD Simulation, SILVACO ATLAS, Interface Recombination, Series Resistance, Shunt Resistance

1. Introduction

Cu(In, Ga)Se_2 (CIGS) solar cells are among the most efficient thin-film photovoltaic technologies, with certified efficiencies exceeding 23% [1]. Their conventional architecture consists of a p-type CIGS absorber combined with an n-type buffer layer, most commonly cadmium sulfide (CdS). Although CdS provides favorable band alignment and effective interface passivation, its use raises environmental concerns due to cadmium toxicity. Moreover, its bandgap (~2.42 eV) can lead to parasitic absorption in the short-wavelength region of the solar spectrum, thereby reducing the photocurrent [2].

In this context, indium sulfide (In_2S_3) has emerged as a promising Cd-free alternative owing to its wide bandgap, high optical transparency, and good chemical stability, while maintaining competitive device performance in CIGS structures [3] [4]. However, the electrical properties of the buffer layer, particularly the donor concentration, strongly influence carrier transport, recombination mechanisms, and band alignment at the heterojunction, making their optimization essential for device performance.

In this work, the influence of donor concentration in the In_2S_3 buffer layer is investigated using SILVACO ATLAS simulations. The donor concentration is varied from 10^{16} to 7×10^{18} cm^{-3} to evaluate its impact on the key photovoltaic parameters (V_{OC}, J_{SC}, FF, and η), with the objective of identifying the optimal doping conditions for high-performance Cd-free CIGS solar cells.

2. Methodology

The numerical simulations were performed using SILVACO ATLAS, a Technology Computer-Aided Design (TCAD) software widely employed for semiconductor device modeling. The simulation framework is based on the self-consistent solution, in two or three dimensions, of the fundamental equations governing carrier transport in semiconductors, namely Poisson's equation, the continuity equations, and the drift-diffusion transport model [3]-[6].

- **Poisson's Equation**

Poisson's equation relates the electrostatic potential ψ to the space charge density ρ within the device:

$$div(\varepsilon \nabla \psi) = -\rho \tag{1}$$

where ε denotes the local permittivity.

Considering free carriers and ionized impurities, the equation can be expressed as:

$$div(\nabla \psi) = \Delta \psi = -\frac{q}{\varepsilon}\left[p - n + N_D^+ - N_A^-\right] \tag{2}$$

where n and p are the electron and hole concentrations, respectively, N_D^+ and N_A^- are the ionized donor and acceptor densities, and q is the elementary charge.

- **Continuity Equations**

The continuity equations describe the temporal evolution of carrier concentrations as a function of current densities and generation-recombination processes:

$$\frac{\partial n}{\partial t} = \frac{1}{q} div \boldsymbol{J}_n + G_n - R_n \tag{3}$$

$$\frac{\partial p}{\partial t} = -\frac{1}{q} div \boldsymbol{J}_p + G_p - R_p \tag{4}$$

where $\boldsymbol{J}_n$ and $\boldsymbol{J}_p$ represent the electron and hole current densities, G the generation rates, and R the recombination rates.

- **Drift-Diffusion Transport Model**

Carrier transport is described using the drift-diffusion approximation:

$$\boldsymbol{J}_n = qn\mu_n \boldsymbol{E}_n + qD_n \nabla n \tag{5}$$

$$\boldsymbol{J}_p = qp\mu_p \boldsymbol{E}_p - qD_p \nabla p \tag{6}$$

where μ_n and μ_p are the carrier mobilities, D_n and D_p the diffusion coefficients, and $\boldsymbol{E} = -\nabla \psi$ the electric field.

The diffusion coefficients are related to mobilities through the Einstein relation:

$$D_{n,p} = \frac{\mu_{n,p} K_B T}{q} \tag{7}$$

This framework is extensively used in numerical modeling of CIGS solar cells and allows accurate evaluation of the influence of material parameters on photovoltaic performance [6].

2.1. Simulated Cell Structure

The simulated device corresponds to a typical CIGS solar cell architecture:

SLG/Mo (500 nm)/p-CIGS (2 μm)/n-In_2S_3 (50 nm)/i-ZnO (100 nm)/ZnO:Al (300 nm)/metallic front grid.

This configuration reproduces standard high-efficiency CIGS devices and enables isolation of the electronic effects induced by the In_2S_3 buffer layer.

Figure 1 illustrates the functional stacking of the device layers. The molybdenum layer ensures efficient back contact, while the p-type CIGS layer acts as the primary absorber. The n-type In_2S_3 buffer layer controls junction formation and band alignment at the heterointerface. The intrinsic ZnO layer reduces leakage currents, and the ZnO:Al layer serves as a transparent conductive window. This architecture allows any performance variation to be directly attributed to modifications in the donor concentration of the In_2S_3 layer.

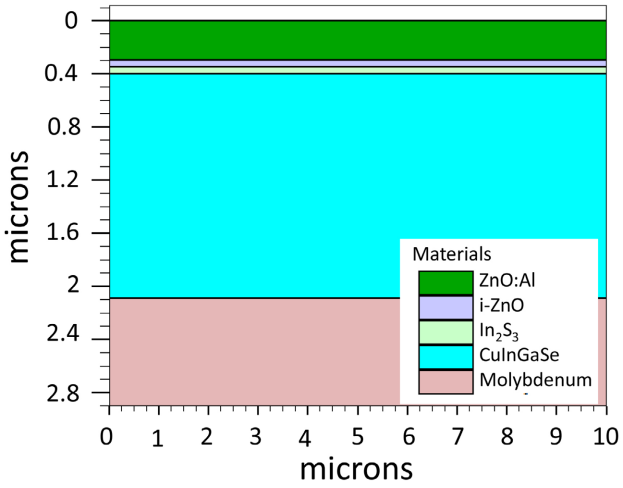

Figure 1. Schematic structure of the CIGS/In_2S_3 solar cell.

2.2. Energy Band Structure of the In_2S_3/CIGS Heterojunction

At thermal equilibrium, the In_2S_3/CIGS interface forms a p-n heterojunction characterized by band bending and the establishment of a built-in electric field. The relative alignment of the conduction and valence bands governs carrier separation and interfacial recombination processes [7] [8].

In this study, the electron affinity and bandgap values are fixed according to literature data, leading to a constant band alignment representative of high-efficiency CIGS devices. Under these conditions, the built-in potential promotes the separation of photogenerated carriers, while buffer-layer properties mainly affect transport losses and recombination rates.

The equilibrium band alignment of the In_2S_3/CIGS heterojunction is illustrated in Figure 2, which shows the conduction and valence band profiles and the resulting built-in electric field governing carrier separation and recombination at the interface.

Figure 2 illustrates the equilibrium energy band diagram of the simulated In_2S_3/CIGS structure. The bending of the conduction band (E_C) and valence band (E_V) across the junction reflects the formation of the depletion region and the associated internal electric field. Since all band-structure parameters are kept constant in this work, performance variations arise from donor-concentration-induced changes in carrier density, conductivity and recombination within the In_2S_3 buffer layer.

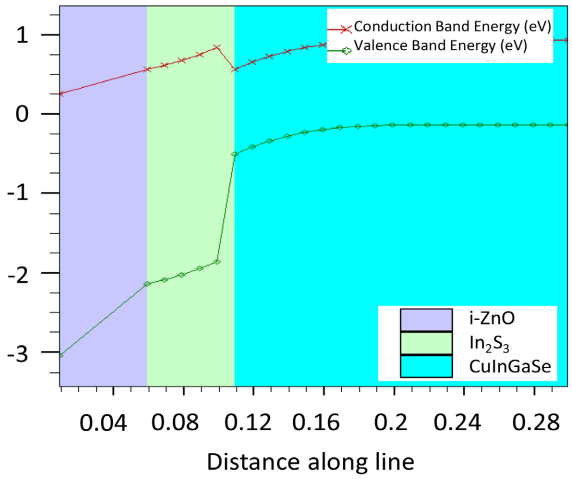

Figure 2. Energy band diagram of the In_2S_3/CIGS heterojunction at equilibrium.

2.3. Simulation Parameters

The numerical simulations conducted in this study are based on a consistent set of physical and electronic parameters accurately describing each layer of the CIGS solar cell. These parameters include fundamental material properties (bandgap energy, electron affinity, dielectric permittivity), geometrical characteristics (layer thickness), as well as carrier transport and recombination quantities (mobilities, carrier lifetimes, effective density of states, and interface trap density).

Table 1. Physical parameters used in the simulations for each layer.

Parameter	ZnO:Al	i-ZnO	In_2S_3	CIGS
Optical bandgap E_g (eV)	3.3	3.3	2.7	1.2
Electron affinity χ (ev)	4.45	4.45	4.2	4.5
Relative dielectric permittivity ε_r	9	9	13.5	13.6
Thickness (μm)	0.3	0.1	0.05	2
Effective density of states N_C (cm^{-3})	2.2×10^{18}	2.2×10^{18}	2×10^{19}	2.2×10^{18}
Effective density of states N_V (cm^{-3})	1.8×10^{19}	1.8×10^{19}	2×10^{17}	1.8×10^{19}
Donor concentration N_D (cm^{-3})	10^{20}	10^{15}	10^{17}	-
Acceptor concentration N_A (cm^{-3})	-	-	-	5×10^{16}
Electron mobility μ_n ($cm^2 \cdot V^{-1} \cdot S^{-1}$)	100	100	50	100
Hole mobility μ_p ($cm^2 \cdot V^{-1} \cdot S^{-1}$)	25	25	15	25
Electron lifetime τ_n (S)	10^{-10}	10^{-10}	10^{-9}	10^{-7}
Hole lifetime τ_p (S)	10^{-10}	10^{-10}	10^{-9}	10^{-7}
Interface defect density D_{it} ($cm^{-2} \cdot ev^{-1}$)	-	-	8×10^{11}	-

The selected values were extracted from well-established literature sources and correspond to high-efficiency CIGS devices, while ensuring numerical stability and convergence within the ATLAS simulation environment. The simulation parameters are listed in **Table 1** [3] [7] [9].

The interface trap density D_{it} was selected within realistic ranges to model partially passivated heterointerfaces, consistent with experimental data reported for high-quality CIGS devices [10] [11].

The optical constants (real and imaginary parts of the complex refractive index $\tilde{n} = n(\lambda) + ik(\lambda)$) of ZnO:Al, i-ZnO, and In_2S_3 were extracted from literature sources [12]-[14], ensuring accurate optical absorption and carrier generation modeling.

2.4. Extracted Photovoltaic Parameters

The current-voltage (J-V) characteristics were simulated under standard AM1.5G illumination (100 mW·cm^{-2}) at room temperature (300 K).

The extracted photovoltaic parameters include:

- **Short-Circuit Current Density (J_{SC})**

The short-circuit current density corresponds to the current generated per unit area when $V = 0$. It can be expressed as:

$$J_{SC} = q\int_0^{\lambda_g} I_0(\lambda)\frac{hc}{\lambda}EQE(\lambda)\mathrm{d}\lambda \tag{8}$$

where $I_0(\lambda)$ is the incident spectral irradiance, h is Planck's constant, c the speed of light in vacuum, $EQE(\lambda)$ the external quantum efficiency, and q the elementary charge.

- **Open-Circuit Voltage (V_{oc}):**

The open-circuit voltage is defined at $J = 0$:

$$V_{OC} = \frac{nkT}{q}\cdot\ln\left(\frac{J_{SC}}{J_0}+1\right) \tag{9}$$

where n is the diode ideality factor, k Boltzmann's constant, T the absolute temperature, and J_0 the saturation current density.

- **Fill Factor (FF)**

The fill factor reflects the electrical quality of the solar cell and is defined as:

$$FF = \frac{J_m \times V_m}{J_{SC} \times V_{OC}} \tag{10}$$

where J_m and V_m correspond to the maximum power point.

- **Conversion Efficiency (η)**

The power conversion efficiency is defined as:

$$\eta = \frac{P_m}{P_{in}} = FF\cdot\frac{J_{SC}\times V_{OC}}{P_{in}} \tag{11}$$

where P_m is the maximum output power and P_{in} the incident optical power density [15].

- **Series and Shunt Resistances**

The series resistance R_s and shunt resistance R_{sh} were determined from the differential resistance:

$$R_{diff} = \left(\frac{\mathrm{d}I}{\mathrm{d}V}\right)^{-1} \tag{12}$$

evaluated near $V \approx V_{OC}$ for R_s, and near $V \approx 0$ for R_{sh} [16].

This approach provides a realistic estimation of resistive losses, capturing the combined effects of carrier transport, recombination, and ohmic contributions.

2.5. Simulation Campaign

A single simulation campaign was performed to investigate the influence of the donor concentration N_D in the In_2S_3 buffer layer.

The donor concentration was varied from 10^{16} to 7×10^{18} cm^{-3} (15 values), covering low, intermediate, and high doping regimes. This range allows the exploration of the trade-off between improved electrical conductivity at moderate doping levels and enhanced recombination mechanisms at high carrier densities.

All other material parameters, including electron affinity, bandgap energy, mobilities, and interface properties, were kept constant throughout the simulations to isolate the specific impact of donor concentration on photovoltaic performance.

3. Results and Discussion

3.1. Overview of the Results

Table 2 summarizes the photovoltaic parameters extracted for the fifteen donor concentrations (N_D) investigated in the In_2S_3 buffer layer. The results clearly reveal a non-monotonic response of device performance as a function of doping concentration. Increasing N_D initially improves carrier collection and resistive parameters, but beyond a critical threshold, performance degradation occurs, mainly driven by a pronounced decrease in the open-circuit voltage V_{OC}.

This behavior reflects a trade-off between:

1) improved electrical conductivity of the buffer layer, and

2) enhanced recombination mechanisms (bulk and interface) at high doping levels, which increase the saturation current density and reduce the open-circuit voltage [15] [17].

Table 2. Photovoltaic parameters as a function of donor concentration in In_2S_3.

Concentration N_D (cm^{-3})	J_{sc} (mA/cm²)	V_{oc} (V)	FF (%)	η (%)	R_s (Ω·cm²)	R_{sh} (Ω·cm²)
10^{16}	29.852	0.828	67.1	16.6	1.93	259
2×10^{16}	30.530	0.815	70.9	17.6	1.74	342
3×10^{16}	31.048	0.802	74.0	18.4	1.61	453

Continued

4×10^{16}	31.446	0.791	76.2	19.0	1.53	590
5×10^{16}	31.762	0.778	77.8	19.2	1.48	722
6×10^{16}	32.047	0.765	78.6	19.3	1.46	738
7×10^{16}	32.391	0.751	78.6	19.1	1.45	534
10^{17}	35.070	0.702	72.8	17.9	1.51	179
2×10^{17}	35.791	0.576	74.3	15.3	1.30	458
5×10^{17}	30.169	0.567	81.9	14.0	1.26	183,264
7×10^{17}	30.157	0.567	81.9	14.0	1.25	380,894
10^{18}	30.150	0.567	82.0	14.0	1.25	433,915
2×10^{18}	30.139	0.566	82.0	14.0	1.24	533,618
5×10^{18}	30.132	0.566	82.0	14.0	1.24	992,457
7×10^{18}	30.131	0.566	82.0	14.0	1.24	1.30×10^{6}

3.2. Impact on Power-Voltage (P-V) Characteristics

Figure 3 shows the simulated P(V) curves for six representative donor concentrations. All curves exhibit the expected parabolic shape with a clearly defined maximum power point (MPP).

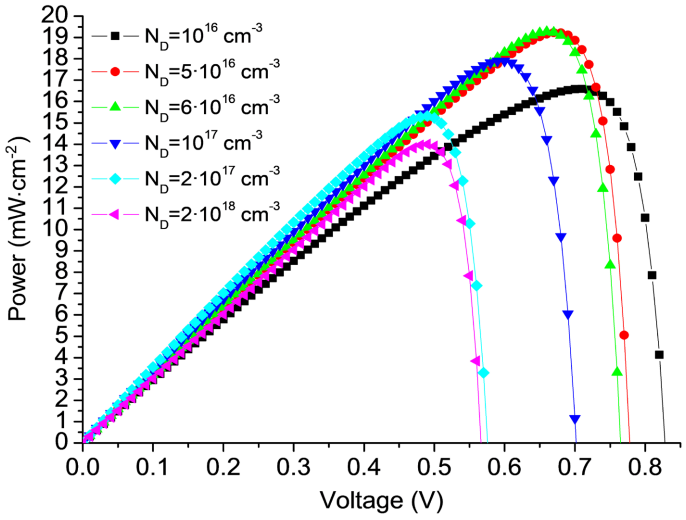

Figure 3. P-V characteristics for different donor concentrations.

A clearly non-monotonic trend is observed.

At low concentration (N_D = 10^{16} cm^{-3}), the maximum output power reaches approximately:

$$P_{max} = 16.5\ \mathrm{mW/cm^2}$$

at

$$V_m = 0.71\ \text{V}$$

As the concentration increases to 6×10^{16} cm^{-3}, the performance significantly improves, and the maximum power reaches:

$$P_{\max} = 19.3\ \text{mW/cm}^2$$

corresponding to an increase of approximately 17%. This value represents the optimal doping level for this simulation series.

Beyond this point, the performance deteriorates sharply. For $N_D \geq 2 \times 10^{17}$ cm^{-3}, the maximum power decreases to approximately 14 mW/cm^2, representing a loss of nearly 27% compared to the optimum.

Simultaneously, the voltage at maximum power V_m decreases from about 0.71 V to 0.48 V, consistent with the observed reduction in V_{OC}.

This evolution highlights the competition between two opposing effects:

- At low doping levels, limited conductivity restricts carrier extraction.
- At intermediate doping, improved electrical conductivity and reduced series resistance enhance carrier transport.
- At high doping levels, performance degradation becomes dominated by enhanced recombination mechanisms (bulk and interface), which increase the saturation current density and significantly reduce V_{OC} [15] [17].

Thus, the improvement in $P_{\max}$ is mainly driven by the increase in J_{SC} and *FF*, whereas the degradation is primarily governed by the reduction of V_{OC}.

3.3. Impact on Current-Voltage (J-V) Characteristics

Figure 4 presents the J-V characteristics under AM1.5G illumination, showing the systematic evolution of photovoltaic parameters with increasing donor concentration in the In_2S_3 buffer layer.

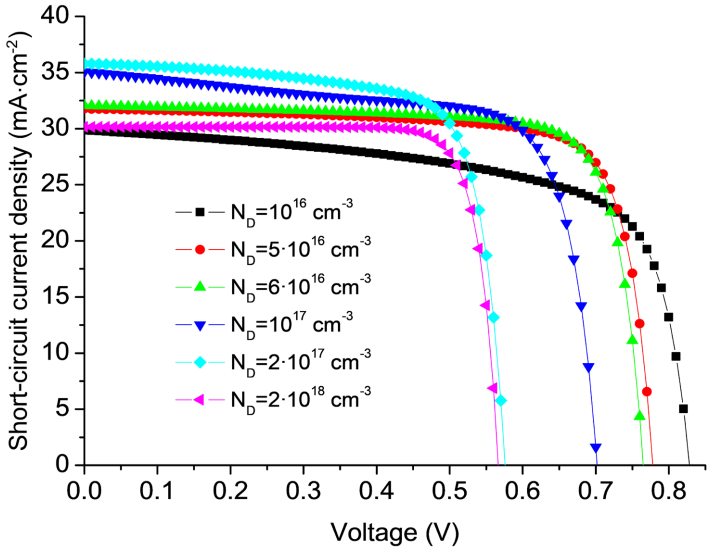

Figure 4. J-V characteristics for different donor concentrations.

The short-circuit current density initially increases from: 29.9 mA/cm^2 at 10^{16} cm^{-3}, to a maximum of:

35.8 mA/cm^2 at 2×10^{17} cm^{-3}, corresponding to an improvement of approximately 20%.

This enhancement is attributed to the increase in buffer-layer conductivity, which facilitates electron transport toward the junction and reduces resistive losses associated with the series resistance [17].

However, beyond this concentration, J_{SC} abruptly decreases and stabilizes around 30.1 mA/cm^2, indicating the onset of a dominant limiting mechanism such as enhanced recombination or unfavorable band alignment.

In contrast, the open-circuit voltage continuously decreases from 0.828 V to approximately 0.566 V, corresponding to a reduction of about 32%.

This pronounced degradation constitutes the main limiting factor at high doping levels. According to the Shockley relation, V_{OC} depends logarithmically on the ratio J_{SC}/J_0 ; therefore, any increase in the saturation current density J_0 (which indicates that recombination is dominated by near-ideal mechanisms, likely radiative or diffusion-controlled processes, as supported by the extracted ideality factor close to unity) directly leads to a reduction in V_{OC} [15] [18].

The results suggest that, at high donor concentrations:

- Recombination processes become increasingly dominant,
- Enhanced carrier recombination reduces the quasi-Fermi level splitting under illumination,
- The effective built-in potential may decrease due to modifications in band bending at the heterojunction,
- The reduced separation of the quasi-Fermi levels ultimately results in a lower open-circuit voltage.

An analysis of the J-V curve shape reveals that:

- At low doping levels, the transition around the knee region is smoother,
- At high doping levels, the transition becomes sharper, reflecting an improved fill factor (associated with lower R_s and higher R_{sh}).

However, this improvement in *FF* remains insufficient to compensate for the strong reduction in V_{OC}, confirming that V_{OC} is the dominant parameter controlling overall device efficiency.

3.4. Influence on the Open-Circuit Voltage V_{OC}

Figure 5 illustrates the evolution of the open-circuit voltage as a function of donor concentration N_D (logarithmic scale). Two distinct regimes clearly emerge: a gradual decrease for $N_D \leq 7 \times 10^{16}$ cm^{-3}, followed by a sharp drop and eventual quasi-saturation at high concentrations.

In the low-to-moderate concentration range (10^{16} to 7×10^{16} cm^{-3}), V_{OC} decreases almost linearly with $\log(N_D)$, dropping from 0.828 V to 0.751 V. This reduction primarily reflects modifications in band alignment at the In_2S_3/CIGS heterojunction, as well as a progressive increase in recombination mechanisms.

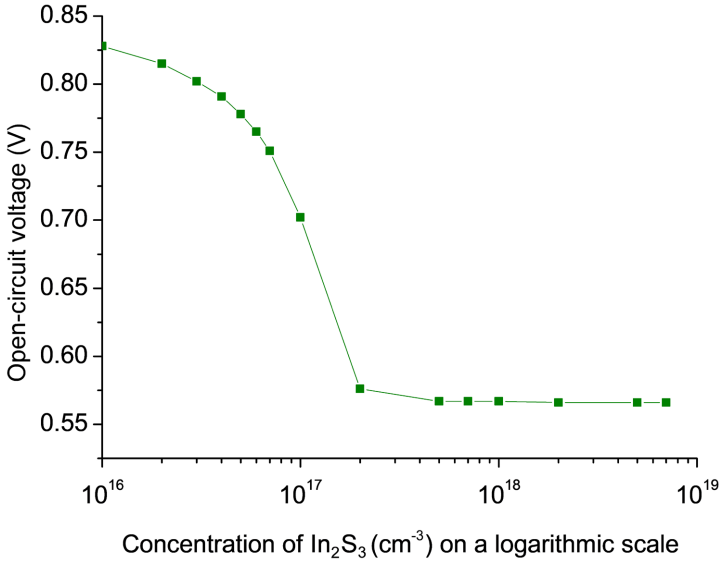

Figure 5. Open-circuit voltage as a function of donor concentration.

For $N_D \geq 7 \times 10^{16}$ cm^{-3}, the decrease becomes much more pronounced: V_{OC} reaches only 0.576 V at $N_D = 2 \times 10^{17}$ cm^{-3}. At even higher concentrations ($\geq 2 \times 10^{18}$ cm^{-3}), V_{OC} stabilizes around 0.566 V, indicating that recombination mechanisms have reached a quasi-steady dominant regime.

This drastic degradation of V_{OC} is mainly attributed to the increase in the saturation current density J_0. According to the Shockley relation, an increase in J_0 leads to a logarithmic reduction of the open-circuit voltage V_{OC} [16]. Several mechanisms may contribute to this increase.

- **Bandgap renormalization (BGN)** at high doping levels may reduce the effective bandgap of In_2S_3 through many-body interactions, potentially dominating over the Burstein-Moss band-filling effect, which normally produces a blue shift [17];
- **Enhanced bulk recombination**, particularly Auger recombination at high carrier densities, which increases the recombination current and contributes to a higher J_0;
- **Modification of the heterojunction barrier**, which can alter the band alignment at the In_2S_3/CIGS interface and reduce the quasi-Fermi level splitting under illumination;
- **Reduction of the effective built-in potential**, resulting from bandgap narrowing and Fermi level shifts at high donor concentrations.

These results confirm that V_{OC} is the most sensitive parameter to excessive doping in the buffer layer.

3.5. Influence on Short-Circuit Current Density J_{sc}

Figure 6 presents the variation of J_{SC} as a function of donor concentration. Unlike V_{OC}, which continuously decreases, J_{SC} exhibits a non-monotonic behavior with a well-defined maximum.

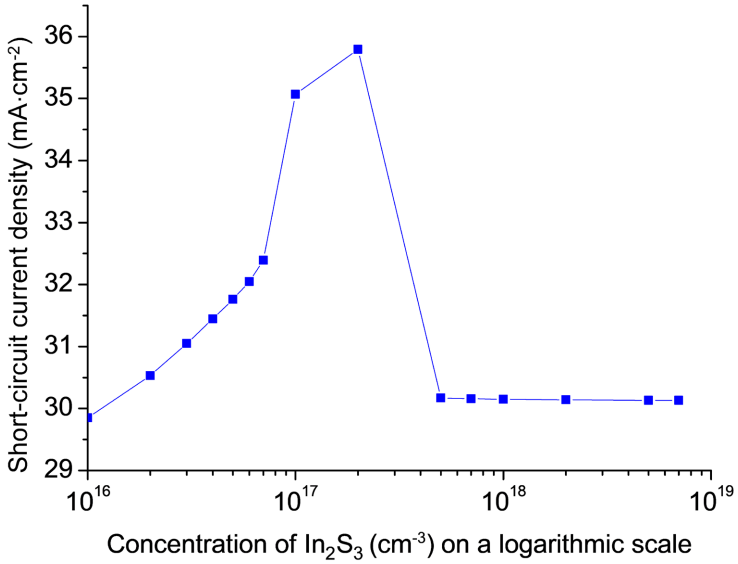

Figure 6. Short-circuit current density as a function of donor concentration.

In the range 10^{16} to 2×10^{17} cm^{-3}, J_{SC} increases from 29.9 to 35.8 mA·cm^{-2} (approximately 20% improvement). This enhancement is explained by:

- Increased electrical conductivity of the In_2S_3 buffer layer;
- Reduced series resistance R_s (from 1.93 to 1.30 Ω·cm^2);
- More efficient extraction of photogenerated electrons.

Beyond 2×10^{17} cm^{-3}, J_{SC} abruptly decreases and stabilizes near 30.1 mA·cm^{-2}. This degradation coincides with the sharp decline in V_{OC}, indicating the emergence of a dominant limiting mechanism.

Several mechanisms may contribute to this behavior:

- Increased bulk and interface recombination;
- Unfavorable modification of the band alignment at the heterojunction;
- Reduction of the space-charge region width, which intensifies the internal electric field and may promote carrier velocity saturation [19];
- Reduction of the minority carrier diffusion length in the CIGS absorber [18].

Notably, the concentration maximizing J_{SC} (2×10^{17} cm^{-3}) is higher than the concentration maximizing overall efficiency (6×10^{16} cm^{-3}). This confirms that final device performance is primarily governed by V_{OC}, rather than J_{SC}.

3.6. Influence on Fill Factor (*FF*)

Figure 7 shows the evolution of the fill factor as a function of donor concentration. The *FF*, which reflects the squareness of the J-V curve, exhibits three distinct regimes.

1) Low concentration regime (10^{16} to 7×10^{16} cm^{-3})

The *FF* increases steadily from 67.1% to 76.2%. This improvement reflects the reduction in R_s and improved carrier transport.

2) Intermediate regime (7×10^{16} to 2×10^{17} cm^{-3})

Significant fluctuations are observed: the fill factor reaches a maximum of

78.6% at 7×10^{16} cm^{-3}, followed by a decrease to 72.8% at 10^{17} cm^{-3}, likely associated with the emergence of parasitic conduction paths, as reflected by the decrease of R_{sh} to 179 Ω·cm^2. The fill factor then increases again to 74.3% at 2×10^{17} cm^{-3}. These variations reveal a competition between resistive losses, leakage currents, and recombination processes that collectively influence the electrical quality of the heterojunction.

3) High concentration regime (≥5×10^{17} cm^{-3})

The FF reaches a high plateau (≈ 82%). This improvement results from:

- Significant reduction in R_s (≈1.24 Ω·cm^2);
- Dramatic increase in R_{sh};
- Reduced leakage currents.

However, despite this high *FF*, the overall efficiency remains limited due to the simultaneous severe degradation of V_{OC}. This underscores the dominant role of recombination mechanisms over purely resistive improvements.

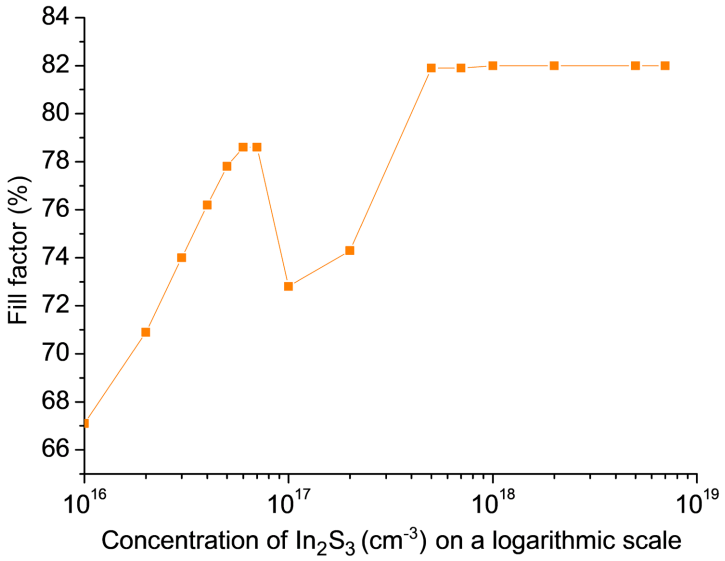

Figure 7. Fill factor as a function of donor concentration.

3.7. Influence on Conversion Efficiency (η)

Figure 8 illustrates the evolution of the power conversion efficiency as a function of donor concentration in the In_2S_3 buffer layer. This parameter, resulting from the combined contribution of J_{SC}, V_{OC}, and the fill factor (*FF*), represents the overall performance indicator of the photovoltaic device.

The obtained profile exhibits a characteristic bell-shaped curve, clearly revealing the existence of an optimal doping level. At low donor concentration (N_D = 10^{16} cm^{-3}), the efficiency remains limited to 16.6%, mainly due to insufficient electrical conductivity in the buffer layer and the resulting high series resistance, which restricts carrier extraction.

As the donor concentration increases, the efficiency progressively improves and reaches a maximum value of 19.3% at $N_D = 6 \times 10^{16}$ cm^{-3}. At this optimal concen-

tration, the three photovoltaic parameters are well balanced:

- $J_{SC} = 32.0\ \text{mA} \cdot \text{cm}^{-2}$,
- $V_{OC} = 0.765\ \text{V}$,
- $FF = 78.6\%$.

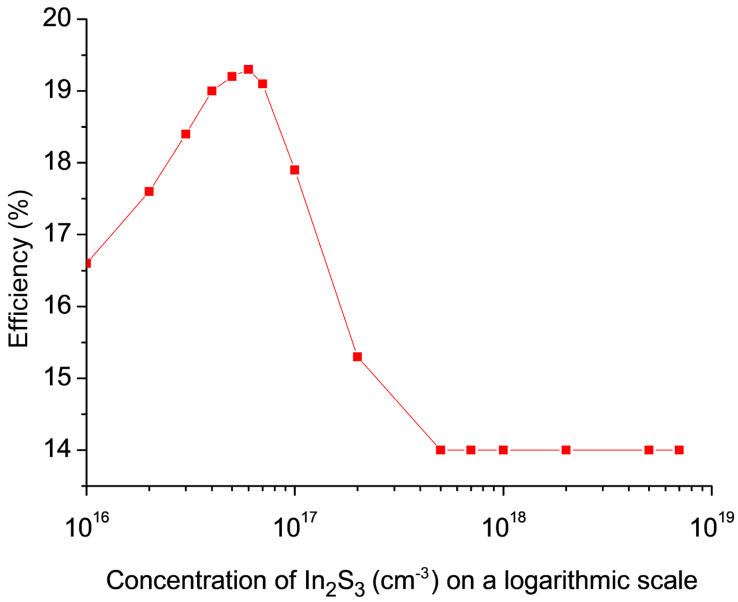

Figure 8. Efficiency evolution as a function of donor concentration.

Beyond this point, the efficiency gradually decreases (17.9% at 10^{17} cm^{-3}, then 15.3% at 2×10^{17} cm^{-3}) and stabilizes around 14.0% at higher concentrations ($N_D \geq 5 \times 10^{17}$ cm^{-3}). This corresponds to an overall loss of approximately 27% compared to the optimum.

This degradation is mainly attributed to the pronounced reduction of V_{OC}, resulting from the combined intensification of recombination processes and modifications of the band alignment at the heterojunction [20] [21]. For low and intermediate donor concentrations, non-ideal recombination mechanisms, mainly Shockley-Read-Hall (SRH), are dominant, as suggested by the extracted ideality factors n around 1.3 - 1.2. At higher concentrations, the ideality factor approaches unity, indicating that more ideal recombination processes, such as radiative and Auger recombination, may become significant.

Recent studies on Cd-free In_2S_3 buffer layers report similar trends, where excessive doping enhances conductivity but deteriorates quasi-Fermi level splitting, ultimately limiting open-circuit voltage and overall device efficiency [22].

The optimal concentration (6×10^{16} cm^{-3}) therefore represents a trade-off between improved carrier transport and controlled recombination losses.

3.8. Influence on Series Resistance (R_s)

Figure 9 shows the variation of the series resistance as a function of donor concentration.

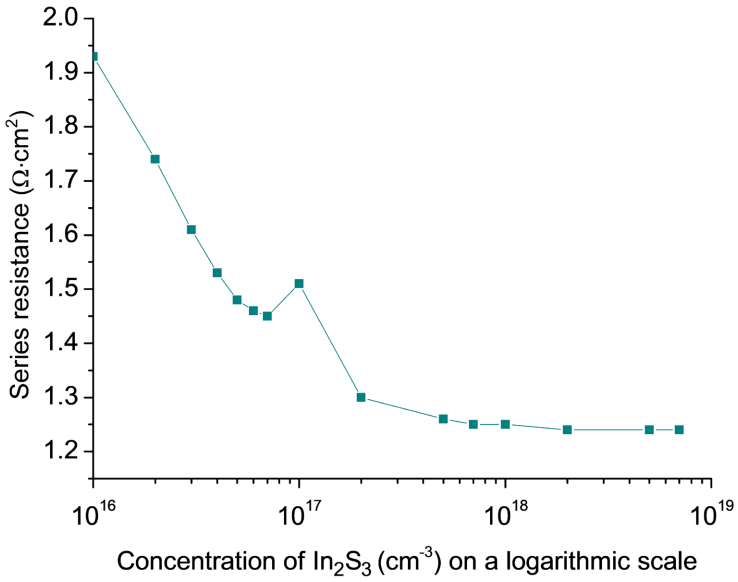

Figure 9. Series resistance as a function of donor concentration.

Overall, R_s decreases as the donor concentration increases, from 1.93 Ω·cm² to 1.24 Ω·cm², corresponding to a reduction of approximately 36%. This trend is directly related to the increase in electrical conductivity of the In_2S_3 buffer layer, described by:

$$\sigma = qn\mu_n \tag{13}$$

where n is the electron concentration and μ_n the electron mobility.

Recent investigations on doped In_2S_3 thin films confirm that increasing carrier density enhances conductivity, although mobility may decrease due to ionized impurity scattering and structural disorder effects [20].

The local anomaly observed in the range 7×10^{16} to 10^{17} cm^{-3} (slight increase in R_s) may therefore result from transient mobility degradation or trap-assisted transport phenomena.

Although the reduction in R_s improves the fill factor, it does not compensate for the simultaneous degradation of V_{OC} at high doping levels. These results confirm that minimizing ohmic losses alone is insufficient to maximize efficiency without controlling recombination processes.

3.9. Influence on Shunt Resistance (R_{sh})

Figure 10 illustrates the evolution of the shunt resistance as a function of donor concentration.

At low doping levels, R_{sh} remains moderate (179 - 738 Ω·cm²), indicating the presence of leakage paths associated with interface defects and trap states.

From 2×10^{17} cm^{-3} onward, R_{sh} increases dramatically, reaching up to 1.3×10^6 Ω·cm² at the highest concentrations. This substantial increase suggests progressive trap filling and apparent improvement in junction quality, a behavior also reported experimentally for highly doped In_2S_3 buffer layers [23].

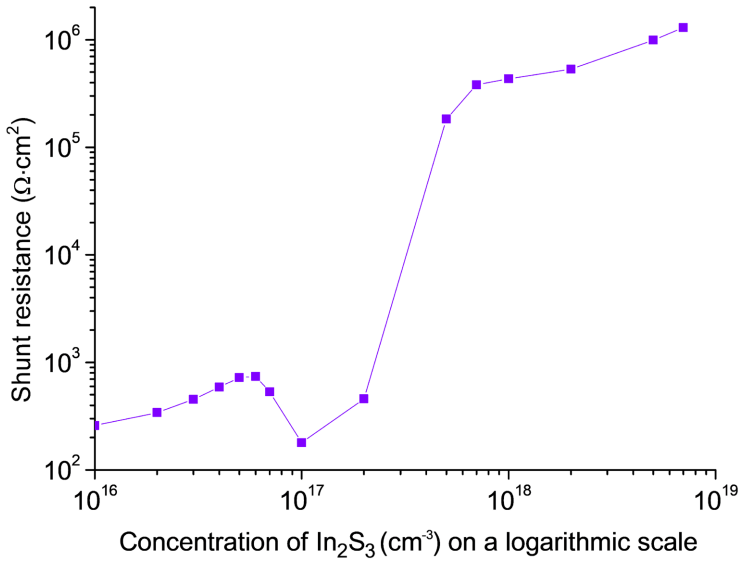

Figure 10. Shunt resistance as a function of donor concentration.

The increase in R_{sh} contributes to the high fill factor (>82%) by suppressing leakage currents. However, despite this resistive improvement, the global efficiency declines due to the dominant reduction in V_{OC}. These findings confirm that recombination processes governing open-circuit voltage are more critical than leakage-current suppression in determining overall device performance.

3.10. Summary

The results demonstrate that the carrier concentration in the In_2S_3 buffer layer has a decisive influence on the performance of the CIGS solar cell.

An optimal compromise is identified at $N_D = 6 \times 10^{16}$ cm^{-3}, allowing a maximum efficiency of 19.3% to be achieved. At this concentration, the improvement in electrical conductivity (reduction of R_s and increase in J_{SC}) still compensates for the losses induced by the progressive intensification of recombination mechanisms.

The overall analysis highlights the dominant role of the open-circuit voltage in determining the final device performance: beyond a certain doping level, the increase in recombination processes outweighs the resistive benefits, irreversibly limiting the overall efficiency of the device.

4. Conclusions

In this work, we conducted a systematic numerical study using the SILVACO ATLAS device simulator to investigate how the donor concentration N_D in the In_2S_3 buffer layer influences the performance of CIGS solar cells. By analyzing the simulated electrical characteristics across a wide doping range (10^{16} to 7×10^{18} cm^{-3}), we established clear correlations between buffer-layer conductivity, recombination losses, and the resulting photovoltaic parameters.

The results reveal the existence of an optimal compromise at $N_D = 6 \times 10^{16}$ cm^{-3},

for which the conversion efficiency reaches $\eta = 19.3\%$. In the low-doping regime, device performance is mainly limited by insufficient buffer conductivity and higher series resistance, which penalize carrier extraction and reduce the fill factor. As N_D increases toward the optimum, enhanced electrical conductivity improves carrier transport, reduces resistive losses, and leads to a net gain in efficiency.

Beyond this optimal level, however, the efficiency progressively decreases and eventually stabilizes at lower values. This degradation is primarily driven by the pronounced reduction of the open-circuit voltage V_{OC}, indicating that recombination-related losses become dominant at high doping levels. Although the fill factor can remain high due to improved resistive parameters, the voltage collapse outweighs these benefits, confirming that V_{OC} is the most critical parameter controlling the global performance within the investigated range.

Overall, these findings demonstrate that optimizing the donor concentration of the In_2S_3 buffer layer is essential to maximize CIGS device efficiency, and that improving transport parameters alone cannot compensate for voltage losses induced by enhanced recombination at excessive doping. Future work should focus on experimental validation of the identified optimal doping window, as well as on advanced characterization of recombination pathways and interface quality to better connect the simulated trends with practical deposition conditions and material stoichiometry control.

Conflicts of Interest

The authors declare no conflicts of interest regarding the publication of this paper.

References

[1] Nakamura, M., Yamaguchi, K., Kimoto, Y., Yasaki, Y., Kato, T. and Sugimoto, H. (2019) Cd-Free Cu(In,Ga)(Se,S)$_2$ Thin-Film Solar Cell with Record Efficiency of 23.35%. *IEEE Journal of Photovoltaics*, **9**, 1863-1867. https://doi.org/10.1109/jphotov.2019.2937218

[2] Hariskos, D., Spiering, S. and Powalla, M. (2005) Buffer Layers in Cu(In,Ga)Se$_2$ Solar Cells and Modules. *Thin Solid Films*, **480**, 99-109. https://doi.org/10.1016/j.tsf.2004.11.118

[3] Sáez-Araoz, R., Krammer, J., Harndt, S., Köhler, T., Krüger, M., Pistor, P., *et al.* (2012) ILGAR In_2S_3 Buffer Layers for Cd-Free Cu(In,Ga)(S,Se)$_2$ Solar Cells with Certified Efficiencies above 16%. *Progress in Photovoltaics: Research and Applications*, **20**, 855-861. https://doi.org/10.1002/pip.2268

[4] Spiering, S., Nowitzki, A., Kessler, F., Igalson, M. and Abdel Maksoud, H. (2016) Optimization of Buffer-Window Layer System for CIGS Thin Film Devices with Indium Sulphide Buffer by In-Line Evaporation. *Solar Energy Materials and Solar Cells*, **144**, 544-550. https://doi.org/10.1016/j.solmat.2015.09.038

[5] Agoundedemba, M., Baneto, M., Nyenge, R., Musila, N. and Toure, K.J.N. (2023) Improving FTO/ZnO/In_2S_3/$CuInS_2$/Mo Solar Cell Efficiency by Optimizing Thickness and Carrier Concentrations of ZnO, In_2S_3 and $CuInS_2$ Thin Films Using Silvaco-Atlas Software. *International Journal of Renewable Energy Development*, **12**, 1131-1140.

https://doi.org/10.14710/ijred.2023.57800

[6] SILVACO Inc. (2010) ATLAS User's Manual/Device Simulation Software Documentation.

[7] Minemoto, T., Hashimoto, Y., Satoh, T., *et al.* (2001) Cu(In,Ga)Se_2 Solar Cells with Controlled Conduction Band Offset of Window/Cu(In,Ga)Se_2 Layers. *Journal of Applied Physics*, **89**, 8327-8330. https://doi.org/10.1063/1.1366655

[8] Taretto, K. and Rau, U. (2008) Numerical Simulation of Carrier Collection and Recombination at Grain Boundaries in Cu(In,Ga)Se_2 Solar Cells. *Journal of Applied Physics*, **103**, Article ID: 094523. https://doi.org/10.1063/1.2917293

[9] Schroder, D.K. (2005) Semiconductor Material and Device Characterization. 3rd Edition, Wiley. https://doi.org/10.1002/0471749095

[10] Shockley, W. and Read, W.T. (1952) Statistics of the Recombinations of Holes and Electrons. *Physical Review*, **87**, 835-842. https://doi.org/10.1103/physrev.87.835

[11] Hall, R.N. (1952) Electron-Hole Recombination in Germanium. *Physical Review*, **87**, 387. https://doi.org/10.1103/physrev.87.387

[12] Carron, R., Avancini, E., Feurer, T., Bissig, B., Losio, P.A., Figi, R., *et al.* (2018) Refractive Indices of Layers and Optical Simulations of Cu(In,Ga)Se_2 Solar Cells. *Science and Technology of Advanced Materials*, **19**, 396-410. https://doi.org/10.1080/14686996.2018.1458579

[13] Esmaili, P. and Asgary, S. (2021) Al^{3+} Doped In_2S_3 Thin Films: Structural and Optical Characterization. *Russian Journal of Inorganic Chemistry*, **66**, 621-628. https://doi.org/10.1134/s0036023621040094

[14] Burstein, E. (1954) Anomalous Optical Absorption Limit in InSb. *Physical Review*, **93**, 632-633. https://doi.org/10.1103/physrev.93.632

[15] Moss, T.S. (1954) The Interpretation of the Properties of Indium Antimonide. *Proceedings of the Physical Society. Section B*, **67**, 775-782. https://doi.org/10.1088/0370-1301/67/10/306

[16] Feneberg, M., Osterburg, G., *et al.* (2014) Band Gap Renormalization and Burstein-Moss Effect in Heavily Doped InN. *Physical Review B*, **90**, Article ID: 075203. https://doi.org/10.1103/PhysRevB.90.075203

[17] Richter, A., Glunz, S.W., Werner, F., Schmidt, J. and Cuevas, A. (2012) Improved Quantitative Description of Auger Recombination in Crystalline Silicon. *Physical Review B*, **86**, Article ID: 165202. https://doi.org/10.1103/physrevb.86.165202

[18] Sah, C.-T., Noyce, R.N. and Shockley, W. (1957) Carrier Generation and Recombination in P-N Junctions and P-N Junction Characteristics. *Proceedings of the IRE*, **45**, 1228-1243. https://doi.org/10.1109/jrproc.1957.278528

[19] Caughey, D.M. and Thomas, R.E. (1967) Carrier Mobilities in Silicon Empirically Related to Doping and Field. *Proceedings of the IEEE*, **55**, 2192-2193. https://doi.org/10.1109/proc.1967.6123

[20] Rau, U. and Schmidt, M. (2001) Electronic Properties of ZnO/CdS/Cu(In,Ga)Se_2 Solar Cells—Aspects of Heterojunction Formation. *Thin Solid Films*, **387**, 141-146. https://doi.org/10.1016/s0040-6090(00)01737-5

[21] Rau, U., Paetel, S. and Werner, J.H. (2003) Band Alignment and Interface Recombination in CIGS-Based Heterojunction Solar Cells. *Physical Review B*, **67**, Article ID: 045203.

[22] Jackson, P., Wuerz, R., Hariskos, D., Lotter, E., Witte, W. and Powalla, M. (2016) Effects of Heavy Alkali Elements in Cu(In,Ga)Se_2 Solar Cells with Efficiencies up to 22.6%.

Physica Status Solidi (*RRL*)—*Rapid Research Letters*, **10**, 583-586.
https://doi.org/10.1002/pssr.201600199

[23] Kato, T., *et al.* (2019) Cu(In,Ga)Se_2 Solar Cell with Efficiency Exceeding 22% and Improved Reproducibility. *IEEE Journal of Photovoltaics*, **9**, 325-330.

Abbreviations

Al: aluminum
AM1.5G: Air Mass 1.5 Global solar spectrum
CdS: Cadmium Sulfide
CIGS: Copper Indium Gallium Selenide (Cu(In, Ga)Se_2)
E_C: Conduction Band Minimum Energy
E_g: Optical Bandgap Energy
EQE: External Quantum Efficiency
E_{vac}: Vacuum Energy Level
E_V: Valence Band Maximum Energy
FF: Fill Factor
In_2S_3: Indium Sulfide
J_{sc}: Short-Circuit Current Density
J-V: Current-Voltage Characteristic
Mo: Molybdenum
N_D: Donor Concentration
η: Power Conversion Efficiency
P-V: Power-Voltage Characteristic
P_{max}: Maximum Output Power
R_s: Series Resistance
R_{sh}: Shunt Resistance
SLG: Soda-Lime Glass
SRH: Shockley-Read-Hall Recombination
TCAD: Technology Computer-Aided Design
V_m: Voltage at Maximum Power Point
V_{OC}: Open-Circuit Voltage
ZnO: Zinc Oxide
χ: Electron Affinity